Nanoscale Advances

ROYAL SOCIETY OF CHEMISTRY

PAPER

View Article Online
View Journal | View Issue

Cite this: *Nanoscale Adv.*, 2023, **5**, 3994

Endometriosis-targeted MRI imaging using bevacizumab-modified nanoparticles aimed at vascular endothelial growth factor†

Qi Zhang,‡[a] Shiman Wu,‡[a] Yajie Li,[a] Mao Lai,[b] Qing Li,[c] Caixia Fu,[d] Zhenwei Yao*[a] and Junhai Zhang *[a]

Endometriosis is a tumor-like disease with high recurrence. In this case, the accurate imaging-based diagnosis of endometriosis can help clinicians eradicate it by improving their surgical plan. However, although contrast agents can improve the visibility of the tissue of interest *in vivo via* magnetic resonance imaging (MRI), the lack of biomarkers in endometriosis hinders the development of agents for its targeted imaging and diagnosis. Herein, aiming at the enriched vascular endothelial growth factor (VEGF) in endometriosis, we developed a targeting MRI contrast agent modified with bevacizumab, *i.e.*, $NaGdF_4$@PEG@bevacizumab–Cy5.5 nanoparticles (NPBCNs), to detect endometriosis. NPBCNs showed negligible cytotoxicity and high affinity towards VEGF in endometrial cells *in vitro*. Furthermore, NPBCNs generated a strong signal enhancement *in vivo* in endometriosis lesions in rats in T_1-weighted images *via* MRI at 3 days post-injection, as confirmed by the histopathological staining results and fluorescence imaging on the same day. Our approach can enable NPBCNs to target endometriosis effectively, thus avoiding missed diagnoses.

Received 8th November 2022
Accepted 26th May 2023

DOI: 10.1039/d2na00787h

rsc.li/nanoscale-advances

1 Introduction

All women have some degree of backflowing menstrual blood.[1] Subsequently, the exfoliated endometrial cells in backflow menstrual blood may cause the abnormal growth of the endometrial gland and stroma outside the lining of the uterus, resulting in the formation of endometriosis.[2] More than 175 million women worldwide suffer from endometriosis and its complications.[3] Although endometriosis is classified benign and non-cancerous, it is very harmful, exhibiting tumor-like migratory and invasive phenotypes.[4] Women with endometriosis are more likely to undergo recurrent pregnancy losses, while 30% to 50% will be infertile.[5] Moreover, in some cases, ectopic endometrial cells can be life-threatening, causing disseminated intravascular coagulation (DIC)[6,7] and increased risk of ovarian cancers.[8,9] Therefore, the timely and accurate management of endometriosis is of great importance.

Presently, the diagnosis and treatment of endometriosis still largely rely on laparoscopic surgery.[10] However, its ~5 year recurrence rate unsatisfactorily remains 40–50%.[11] Furthermore, postoperative suppressive therapy to treat residual endometriosis may not benefit all patients (such as hindering them from becoming pregnant) and cannot successfully prevent recurrence. Therefore, localizing the precise range of endometriosis for the development of a surgical plan will improve the outcome of endometriosis patients in the long term. Currently, magnetic resonance imaging (MRI) is the preferred non-surgical technique for the diagnosis of endometriosis. The clinical gadolinium (Gd)-based MRI contrast agents are used for enhancing the visibility of the tissue of interest.[12] Specifically, this contrast agent can diffuse faster in tumors with dense tumor capillaries, leading to the better enhancement of the tumor relative to the surrounding tissue. However, given that endometriosis exhibits infiltrating growth without evident boundaries, clinical MRI contrast agents are non-targeting and thus cannot reveal the whole scope for the precise development of a surgical plan. Therefore, an MRI contrast agent targeting endometriosis can effectively help clinicians delineate the extent of surgical resection precisely.

Herein, we developed targeting nanoparticles as an MRI contrast agent to achieve the precise imaging of endometriosis (Fig. 1). Vascular endothelial growth factor (VEGF) is enriched in ectopic endometrium.[13,14] In this case, bevacizumab, as a monoclonal antibody, can specifically target VEGF.[15] Therefore, bevacizumab-modified nanoparticles have potential to

[a]*Department of Radiology, Huashan Hospital, Fudan University, Shanghai 200040, P.R. China. E-mail: jhzhang007@fudan.edu.cn; zwyao@fudan.edu.cn*

[b]*Department of Radiology, The First People's Hospital of Jinghong, Jinghong City, Yunnan Province, P.R. China*

[c]*MR Collaborations, Siemens Healthineers Digital Technology (Shanghai) Co., Ltd, Shanghai, China*

[d]*MR Application Development, Siemens Shenzhen Magnetic Resonance Ltd, Gaoxin C. Ave, 2nd, Hi-Tech Industrial Park, Shenzhen, 518057, China*

† Electronic supplementary information (ESI) available: Additional file 1. Supplementary figures. Fig. S1–S3. See DOI: https://doi.org/10.1039/d2na00787h

‡ The two authors contributed equally to this work.

effectively target endometriosis lesions *in vivo*. $NaGdF_4$ nanoparticles were chosen as the core material of the bevacizumab-modified nanoparticles for several reasons. Firstly, $NaGdF_4$ nanoparticles are biocompatible,[16] indicating that they can be used in biomedical applications without causing adverse effects. Secondly, $NaGdF_4$ nanoparticles contain gadolinium (Gd), a paramagnetic metal that has a strong ability to alter the relaxation times of water molecules in its vicinity, leading to a brighter signal in MRI images. This enables $NaGdF_4$ nanoparticles to serve as T_1 imaging contrast agents with high relaxivity,[17,18] reducing the required dosage of contrast agent. Thirdly, $NaGdF_4$ nanoparticles have a high surface area to volume ratio,[19] which enables them to carry a large number of targeting ligands on their surface for the specific targeting of tissues or cells, thereby allowing the more precise imaging of the targeted lesion.[20] Overall, the combined biocompatibility, paramagnetic properties, and high surface area to volume ratio for modification of $NaGdF_4$ nanoparticles make them an excellent candidate for targeted MRI. The $NaGdF_4$@PEG@bevacizumab–Cy5.5 nanoparticles (NPBCNs) reported herein provide a strategy for combing anti-VEGF antibodies and biocompatible nanoparticles, which will inspire the targeted molecular imaging of endometriosis.

2 Results and discussion

2.1 Characterization

Briefly, the process for the synthesis of two types of nanoparticles, NPBCNs and NPCNs, is illustrated in Fig. 1. Firstly, oleic acid-stabilized $NaGdF_4$ nanoparticles were synthesized through a thermal decomposition process, as previously described,[21] and subsequently modified with PEG–cholesterol, bevacizumab and Cy5.5 for hydrophilicity, endometriosis-targeting and fluorescence tracking, respectively. Transmission electron microscopy (TEM) (Fig. 2a) confirmed the successful preparation of the $NaGdF_4$ nanoparticles and NPBCNs, demonstrating their uniform spherical morphology. The crystallite size and phase formation of $NaGdF_4$ nanoparticles, $NaGdF_4$@PEG–NHS–Cy5.5 nanoparticles (NPCNs) and NPBCNs were identified and confirmed by comparing the data with the standard JCPDS X-ray diffraction (XRD) patterns (Fig. 2b). The diffraction peaks located at the 2θ values of 29.8°, 42.5° and 52.5° for NPBCNs and NPCNs corresponded with the characteristic (101), (201) and (211) diffraction peaks in the $NaGdF_4$ standard spectrum, respectively. The broad XRD peaks of NPBCNs and NPCNs at around 18° and 23° are associated with the PEG crystal. Furthermore, Fourier transform infrared (FT-IR) spectroscopy verified the successful surface modification of the nanoparticles (Fig. 2c), especially the stretching vibration of C=O at 1734 cm^{-1}, vibrations of C–O–C at 1113 cm^{-1} and out-of-plane bending vibration of O–H at around 963 cm^{-1}. The T_1 imaging ability of NPBCNs, *i.e.*, relaxivity (r_1), was measured on a 3T MR platform and the analytic results plotted in Fig. 2d. The images of the gradient concentration of NPBCNs exhibited a concentration-dependent effect. NPBCNs exhibited a high r_1 longitudinal relaxivity of 7.65 mm^{-1} s^{-1}, which is about two-fold that of the clinically used MRI contrast agents *Magnevist* (r_1 = 3.8 mM^{-1} s^{-1})[22] and *Omniscan* (r_1 = 3.3 mM^{-1} s^{-1}).[23] Notably, a high relaxivity minimizes the dosage of contrast agents, while satisfying the contrast enhancement requirement, reducing the risk of potential side effects. Dynamic light scattering (DLS) examination showed a narrow particle size distribution with an average of 139.2 nm (Fig. S1, ESI†).

2.2 Cellular uptake

The cytotoxicity of the nanoparticles was evaluated on the human endometrial cell line hEM15A. The cell viability was above 80% at different concentration gradients of NPBCNs. The targeted NPBCNs showed negligible cytotoxic effects toward hEM15A cells (Fig. S2, ESI†).

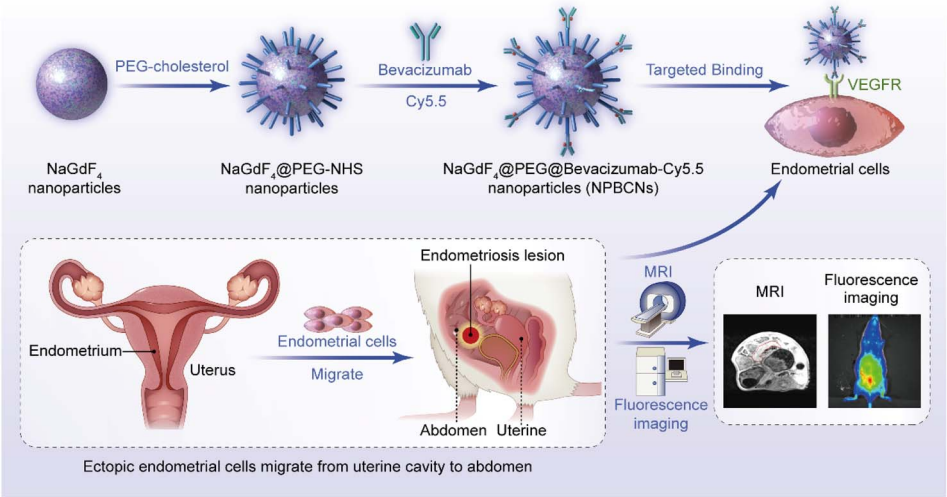

Fig. 1 Schematic illustration of the facile synthesis of $NaGdF_4$@PEG@bevacizumab–Cy5.5 nanoparticles (NPBCNs) and their biomedical application as a contrast agent for MRI and fluorescence imaging for the diagnosis of endometriosis.

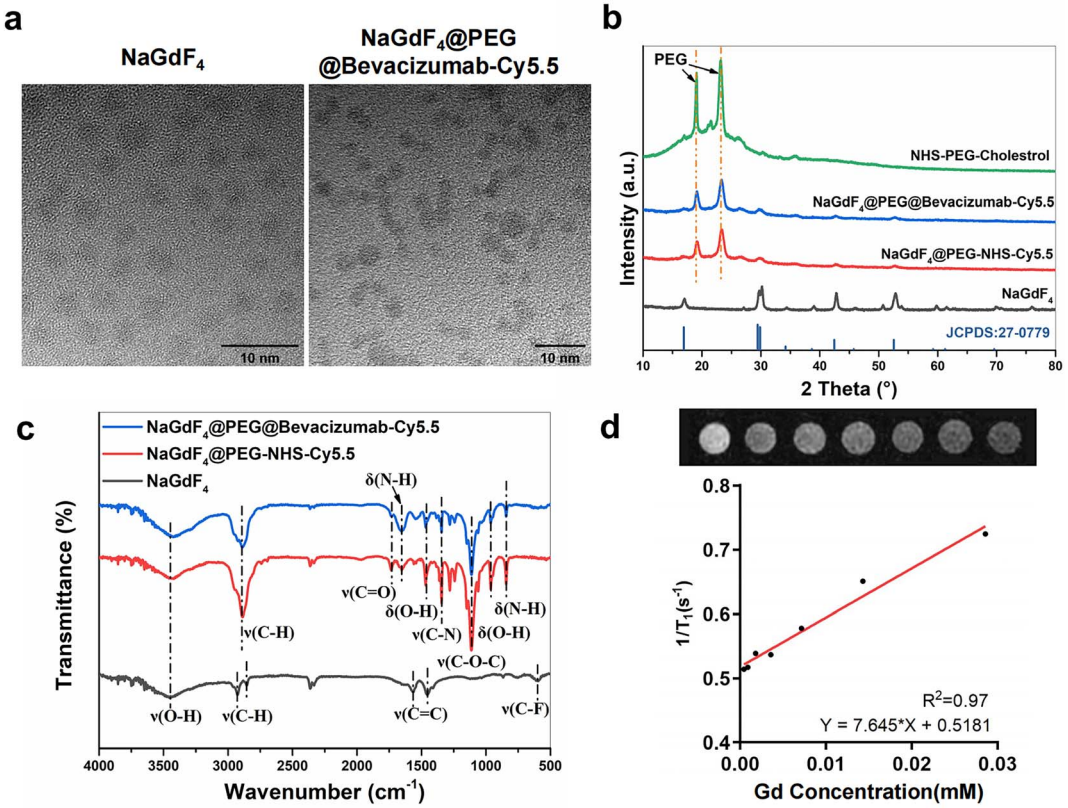

Fig. 2 Characterization of $NaGdF_4$@PEG@bevacizumab–Cy5.5 nanoparticles (NPBCNs). (a) Transmission electron microscopy (TEM) images of $NaGdF_4$ nanoparticles and NPBCNs. (b) X-ray diffraction (XRD) pattern of NHS–PEG–cholesterol, NPBCNs, $NaGdF_4$@PEG–NHS–Cy5.5 nanoparticles (NPCNs) and $NaGdF_4$ nanoparticles. (c) Fourier transformation infrared (FTIR) spectra of $NaGdF_4$ nanoparticles, NPCNs, NPBCNs. (d) T_1-Weighted MR imaging of NPBCNs at different concentrations of Gd and the T_1 relaxivity NPBCNs.

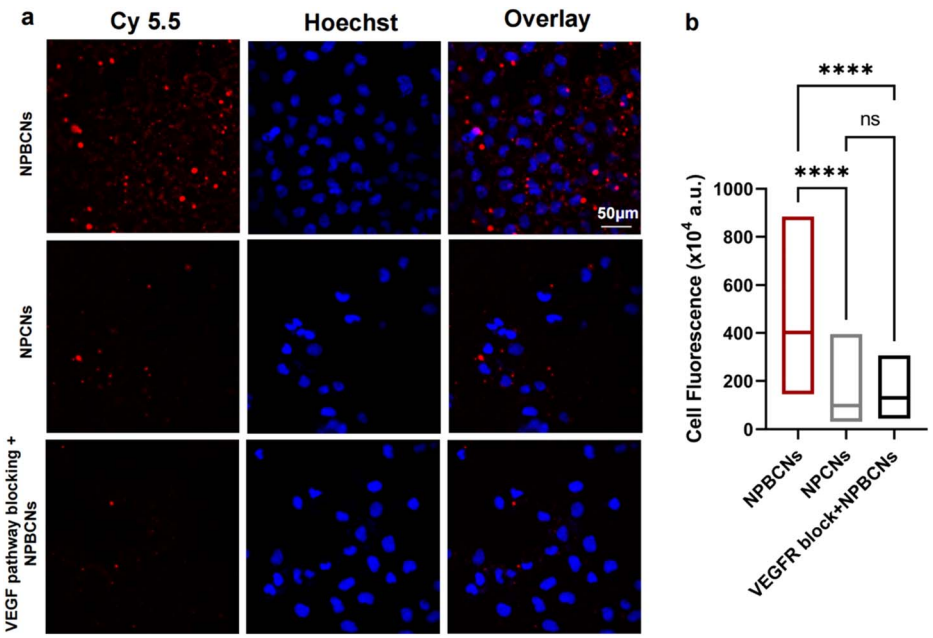

Fig. 3 Representative confocal laser scanning microscopy (CLSM) images and analysis of cellular uptake of nanoparticles in hEM15A endometrial cell line *in vitro*. (a) hEM15A cells incubated with $NaGdF_4$@PEG@bevacizumab–Cy5.5 nanoparticles (NPBCNs) (upper) and $NaGdF_4$@PEG–NHS–Cy5.5 nanoparticles (NPCNs) (middle). After blocking the VEGF signaling pathway with free bevacizumab, hEM15A cells were incubated with NPBCNs (bottom). (b) Quantitative analysis of mean fluorescence intensity in hEM15A cells. ****, $p < 0.001$; ns, non-significant.

Furthermore, given that endometrial cells are the initiator of endometriosis, the subcellular localization of the nanoparticles was examined in endometrial cells *via* confocal laser scanning microscopy (CLSM). The VEGF receptor is highly expressed in hEM15A cells, which can be specifically targeted by bevacizumab. According to the observation through CLSM (Fig. 3), a higher degree of NPBCNs was selectively internalized by hEM15A cells than NPCNs, as revealed by the higher scarlet-fluorescence intensity in the NPBCN-treated cells compared to the NPCN-incubated cells (NPBCNs *vs.* NPCNs: $p < 0.00001$). Besides, the fluorescence intensity significantly decreased when the hEM15A cells were pretreated with excess bevacizumab before the addition of NPBCNs (NPBCNs *vs.* NPBCNs with pretreatment: $p < 0.00001$), demonstrating a similar low fluorescence intensity with the non-targeted NPCNs-incubated cells (NPBCNs with pretreatment *vs.* NPCNs: $p > 0.05$). Taken together, the selective accumulation of targeted NPBCNs is probably due to the outstanding affinity of bevacizumab to VEGF receptor-mediated endocytosis in the hEM15A cells, indicating that NPBCNs can target endometrial cells effectively *in vitro*.

2.3 *In vivo* MRI imaging

All the endometriosis rats were imaged using a 3T MRI system equipped with a specialized rat coil. The endometriosis lesions of each rat presented as a nodule with an iso-intensity signal on T_1 WI. Half of the endometriosis rats were injected with the targeting NPBCNs, while the other half was administrated with

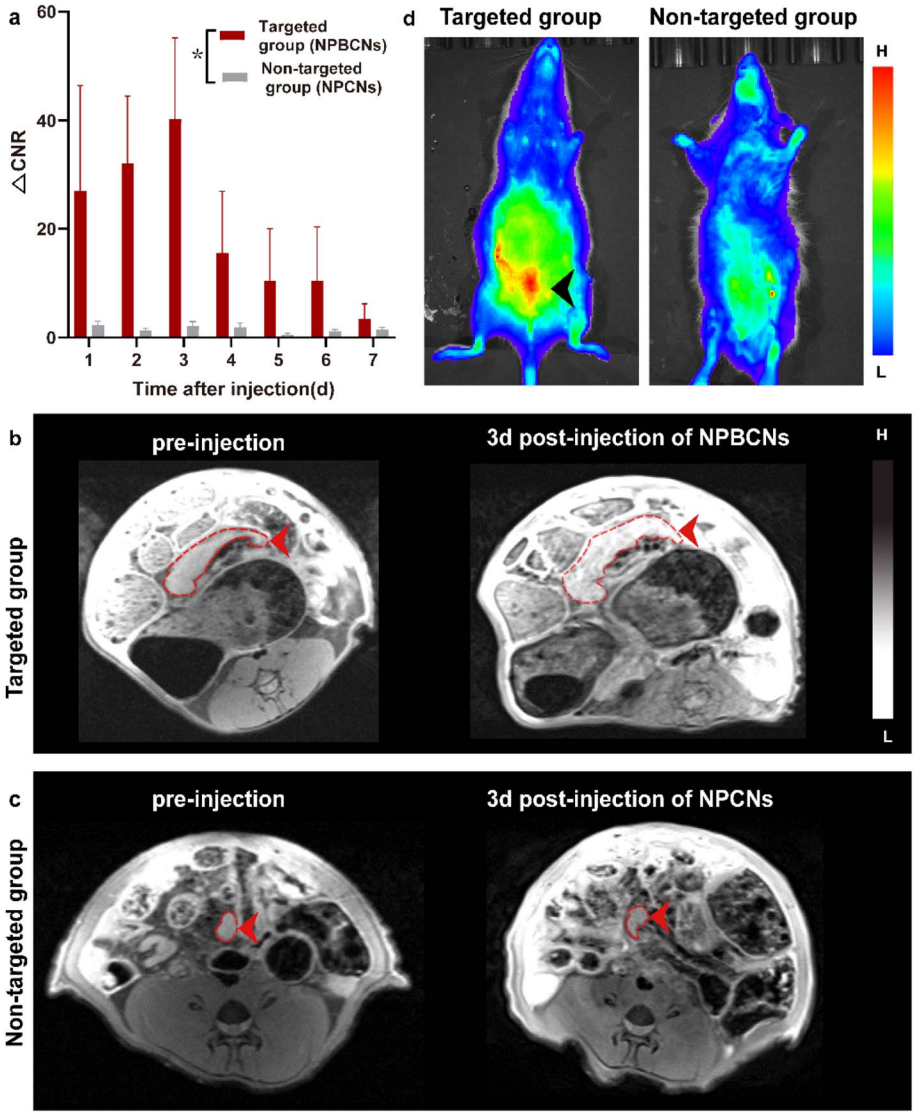

Fig. 4 Targeted imaging performance of $NaGdF_4$@PEG@bevacizumab–Cy5.5 nanoparticles (NPBCNs) in endometriosis rats. (a) MR-signal intensity of the endometriosis lesion in the targeted group and non-targeted group with prolonged duration after intravenous administration (*, $p < 0.05$). (b) Representative T_1-weighted images of rats with endometriosis in the targeted group before and after intravenous injection of NPBCNs. (c) Representative T_1-weighted images of rats with endometriosis in the non-targeted group before and after intravenous injection $NaGdF_4$@PEG–NHS–Cy5.5 nanoparticles (NPCNs). (d) Fluorescence image of the targeted group and the non-targeted group and NPCNs on 3 d post-injection (H = high and L = low).

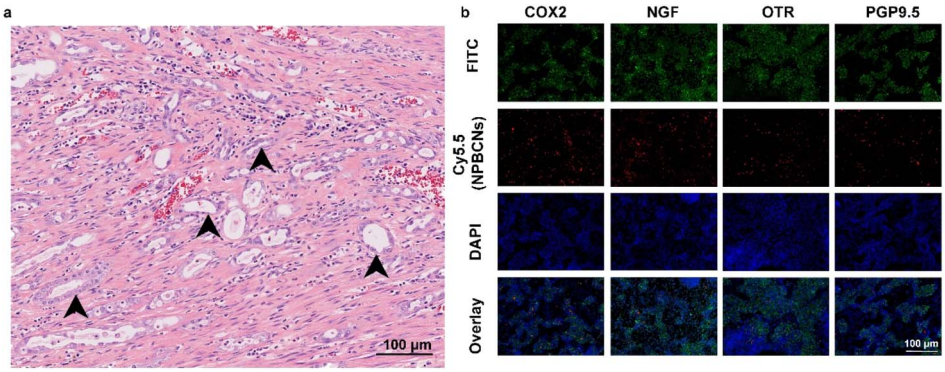

Fig. 5 Histological assessment of endometriosis lesion in the targeted group. (a) Representative histologic image (400×) from of models with endometriosis. (b) Representative colocalization images of endometriosis lesions from rats injected with $NaGdF_4$@PEG@bevacizumab–Cy5.5 nanoparticles (NPBCNs). Cy5.5 channel: NPBCNs; Hoechst channel: cell nuclei and FITC channel: the immunofluorescence staining for the makers for ectopic endometrial cells [cyclooxygenase-2 (COX2) oxytocin receptor (OTR), nerve growth factor (NGF) and PGP9.5].

non-targeting NPCNs, which were denoted as the targeting and non-targeting groups, respectively.

As shown in Fig. 4a, the dynamic change in the two groups after the injection of NPBCNs or NPCNs was investigated quantitatively. The CNR of the endometriosis lesion was calculated as the difference in the signal-to-noise ratio between the endometriosis lesion and muscle regions of interest. The time dependence of the change in CNR ($\Delta CNR = CNR_{pre} - CNR_{post}$) following injection was determined using the sequential MR images. The ΔCNR of the endometriosis lesion in the targeting group was higher than that in the non-targeting group on 1 d post-injection and gradually increased, then reaching the peak at 3 d post-injection. The difference between the targeting group (40.26 ± 14.94) and non-targeting group (2.12 ± 0.84) was approximately the maximum 3 days after NPBCN injection. Besides, the ΔCNR value of the targeted group at each time point was statistically significantly higher than that of the non-targeting group from 1 d to 7 d post-injection ($p = 0.02 < 0.05$). Subsequently, the enhancement in the targeting group began to weaken but sustained visibly until 6 d post-injection.

The time-dependent ΔCNR data was used to determine the optimal imaging time point where the maximum ΔCNR was observed. Herein, 3 d-post injection was set as the optimal imaging time point for the comparison of the image between the two groups. The T_1 signal of the endometriosis lesions in the targeting group manifested an obvious enhancement 3 days after NPBCN injection (Fig. 4b). In contrast, in the non-targeted group, no contrast-enhanced region inside the endometriosis tissue was observed (Fig. 4c) or in other tissue following the injection of NPCNs. It is known that the enhanced permeability and retention (EPR) effect will result in the deposition of non-targeted nanoparticles in tumors.[24,25] Notably, given that endometriosis is a non-tumor disease, the non-targeted NPCNs could not accumulate in the endometriosis tissue to generate a visible enhancement in the T_1-weighted images. In summary, the T_1 signal enhancement in the targeted group resulted from the targeting ability of NPBCNs towards the VEGF signaling pathway of endometriosis.

The fluorescence imaging of the targeting group and the non-targeting group on 3 d post-injection further verified the MRI results (Fig. 4d). The predominant uptake of NPBCNs was observed in the abdomen from coronal projection. Meanwhile, no fluorescein stain was observed in the non-targeting group. Utilizing NPBCNs, the endometriosis-afflicted areas could be successfully delineated, leading to the diagnosis of endometriosis. The above-mentioned results indicate that NPBCNs can serve as an efficient MRI contrast probe for the targeted imaging of endometriosis lesions *in vivo*.

Moreover, histopathological examination confirmed the presence of endometriosis in all the rats. As shown in Fig. 5a, stromal endometrioid and epithelial elements of the Müllerian type were found in their abdominal cavity, surrounded by fibers and stroma. Cyclooxygenase-2 (COX2),[26] oxytocin receptor (OTR),[27] nerve growth factor (NGF) and pan-neuronal marker PGP9.5 (ref. 28) were found to be highly expressed in the cytoplasm of the endometrial cells, which indicated the core area of endometriotic tissues. The bright red fluorescence from NPBCNs showed co-localization with the FITC fluorescence of the endometriotic cells expressing COX-2, OTR, NGF and PGP9.5.

2.4 Biosafety of NPBCNs

The 9 healthy rats injected with NPBCNs or phosphate-buffered saline (PBS) well tolerated the nanoprobes without any short--term (3 days) or long-term (60 days) adverse effects according to the hematological indices as well as histological observation of the heart, liver, spleen, lung, and kidney (Fig. S3a, ESI†). There was no pathological deficit or evident difference between the NPBCN-treated and phosphate-buffered saline (PBS)-treated mice over 60 days (Fig. S3b, ESI†). These results suggest that NPBCNs intrinsically feature excellent biocompatibility for potential clinical translation, especially for further VEGF-targeted T_1-weighted imaging.

3 Conclusions

In summary, NPBCNs synthesized in our study served as a novel MRI contrast agent, which exhibited a high relaxation rate and excellent specificity for endometriosis, filling the blank of targeted imaging for the diagnosis of endometriosis. Owing to its

high affinity to the VEGF receptor in ectopic endometrial cells, NPBCNs served as an efficient MR imaging probe for the accurate detection and targeted imaging of endometriosis lesions. Moreover, it could also be shown in fluorescence images *in vivo*. Besides, given that neovascularity is highly associated with the proliferation of endometriosis, the T_1 signal intensity caused by NPBCNs may be used to quantify the proliferative activity of multiple endometriosis foci and classify the priority during surgical plans in future studies. Additionally, no obvious toxicity or adverse effect of NPBCNs was observed, demonstrating their great biocompatibility. Therefore, NPBCNs can be potentially used for the detection of endometriosis lesions by clinical MRI. It is postulated that NPBCNs have potential application for the accurate medical diagnosis of endometriosis.

4 Experimental

4.1 Materials

Oleic acid and 1-octadecene (90%) were purchased from Sigma-Aldrich. NHS–PEG2000–cholestrol were purchased from Ponsure Biological (Shanghai, China). NaOH, OA and NH_4F were obtained from Damas-beta (Shanghai, China). Cyclohexane and chloroform ($CHCl_3$) were purchased from General-reagent company. All reagents were of analytical grade and used without further purification. RPMI 1640 medium, penicillin–streptomycin solution, fetal bovine serum (FBS) and phosphate buffer saline (PBS) were acquired from Gibco Company (USA). The cell cultivation mixture consisted of RPMI 1640 medium, FBS (10%), and penicillin–streptomycin solution (1%). Sulfo-Cyanine5.5 NH_2 was obtained from Shanghai Maokang Biotechnology Co., Ltd. Bevacizumab was purchased from MedChemExpress (Shanghai, China). Cell Counting Kit 8 assay was purchased from 7Sea Biotech Company (Shanghai, China). Deionized water (DI water, 18.2 MΩ) was acquired from a Milli-Q Millipore Water System (Millipore, MA, USA) and used in all experiments. An AniView 100 living body imaging system (BLT, China) was used to observe Cy5.5 fluorescence from NPBCNs, using the Cy5.5 filter sets (excitation: 673 nm and emission: 707 nm). The near-infrared fluorescent dye Cy5.5 has an emission wavelength beyond the visible range, and the fluorescence pseudocolor assigned to Cy5.5 was red.

4.2 Preparation of $NaGdF_4$ nanoparticles

The OA–$NaGdF_4$ nanoparticles were synthesized as previously described[17] with slight modification. Briefly, after dissolving $GdCl_3 \cdot 6H_2O$ (2 mmol) in DI water, a mixture of 15 mL oleic acid and 30 mL 1-octadecene was added. With magnetic stirring under argon gas, the mixed system was heated to 80 °C and held for 150 min initially, then ramped to 120 °C for 1 h, and finally raised to 160 °C for 1 h. After the system naturally cooled to room temperature, a methanol solution of dissolved NH_4F (0.296 g) and NaOH (0.2 g) was added to the mixed system and stirred for 12 h. Subsequently, the methanol was removed by slowly heating with the following program: warmed to 70 °C and maintained for 1 h, slowly warmed to 80–100 °C and maintained for 1 h, then heated to 140–150 °C and held for 1 h, and finally increased temperature to 260 °C for 1 h under the protection of argon. After, the obtained $NaGdF_4$–OA nanoparticle product was washed with ethanol and cyclohexane (3 : 1) mixture three times, and finally redispersed in chloroform.

4.3 Characterization of $NaGdF_4$@PEG–NHS–Cy5.5 nanoparticles (NPNs)

Briefly, $NaGdF_4$@PEG–NHS nanoparticles were obtained by modifying $NaGdF_4$ particles with amphiphilic cholesterol–PEG–NHS. Firstly, cholesterol–PEG2000–NHS (0.5 g) was dissolved in chloroform. Secondly, the above-mentioned OA–$NaGdF_4$ chloroform solution was mixed with cholesterol–PEG2000–NHS–chloroform solution, and subsequently stirred at room temperature for 12 h. Then, the chloroform was removed by rotary evaporation. Next, the product was dispersed in DI water and collected by centrifugation, and the hydrophilic $NaGdF_4$@PEG–NHS nanoparticles (NPNs) were acquired and stored at 4 °C. Some of NPNs were used for the subsequent synthesis of NPBCNs, and the rest labelled with Cy5.5 for *in vivo* study in the non-targeting group. After sulfo-Cyanine5.5-NH_2 (1 mg) was dissolved in DI water, an $NaGdF_4$@PEG–NHS solution was added and stirred overnight in a dark environment. Then, the Cy5.5-labeled $NaGdF_4$@PEG–NHS–Cy5.5 nanoparticles (NPCNs) were acquired and stored in the dark at 4 °C.

4.4 Preparation of $NaGdF_4$@PEG@bevacizumab–Cy5.5 nanoparticles (NPBCNs)

Firstly, the $NaGdF_4$@PEG–NHS nanoparticles were washed and redispersed in DI water (20 mg Gd mL^{-1}). Secondly, sulfo-Cyanine5.5 NH_2 (1 mg) and bevacizumab (1 mg) were dissolved in DMSO. Thirdly, sulfo-Cyanine5.5 NH_2–DMSO solution and bevacizumab–DMSO solution were mixed with $NaGdF_4$@-PEG–NHS nanoparticles (20 mg) – chloroform solution and stirred at room temperature for 24 h. Then, the product was washed twice by centrifugation and re-dispersed in DI water. Finally, the obtained $NaGdF_4$@PEG@bevacizumab–Cy5.5 nanoparticles (NPBCNs) were cryopreserved and shielded from the light.

4.5 Characterization

TEM imaging was performed on a JEOL 200CX microscope at an accelerating voltage of 200 kV. Powder XRD patterns were measured on a Japanese Rigaku D/MAX-2250V diffractometer. Fourier transform infrared spectroscopy (FT-IR) was performed on a Nicolet Avatar 370 FT-IR spectrophotometer using KBr disks. The Gd concentration of the NPBCN solution was measured by inductively coupled plasma optical emission spectrometry (ICP-OES) after dissolving in aqua regia. The T_1 imaging ability of NPBCNs was determined as T_1 relaxivity (r_1) using a 3.0 T MR scanner (Discovery MR 750, GE Medical Systems, Milwaukee, WI, USA) with an 8-channel head coil. The MR scanning parameters were as follows: gradient TI (50, 100, 150, 200, 300, 400, 800, 1500, and 2000 ms); TE/TR = 7.9 ms/5000 ms; echo train length (ETL) = 8, NEX = 3, bandwidth = ±125 kHz.

4.6 Cytotoxicity assay

The cytotoxicity of NPBCNs was determined using the standard CCK8 assay. The human endometrial cell line hEM15A cells were purchased from YoBi Biotech Co., Ltd and seeded in 96-well plates at a density of 5000 cells per well and cultured with 1640 medium (DMEM, Gibco, USA) containing 10% fetal bovine serum (FBS, Gibco, USA) under 5% CO_2 atmosphere at 37 °C. After 24 h of incubation, the cells were cocultured with $NaGdF_4$@PEG@bevacizumab at various Gd(III) concentrations (100, 200, 500, 1000, 2000, 3000 ppm) for an additional 24 h. After the hEM15A cells were washed three times with PBS to remove the nanoparticles, 10 μL of CCK:8 was added to the cells. Optical densities (OD) were determined at a wavelength of 450 nm using a microplate reader (Biotek, USA).

4.7 Cellular uptake and blockade test

The hEM15A cells were seeded at the density of 5000/1 mL on a CLSM-special cell culture dish and grown to 80% confluency. After 4 h co-incubation of the hEM15A cells with NPBCNs and NPCNs (50 Gd μg mL^{-1}), the labeled cell suspension washed three times with PBS to remove the nanoparticles followed by nuclei staining with Hoechst (Beyotime, Shanghai, China). For the competitive blocking studies, another group of cells was pretreated with excess bevacizumab before the addition of NPBCNs. CLSM images were recorded on FV 1000, Olympus (Japan). A 40× objective lens was used and luminescence signals were detected in the wavelength range for Cy5.5 (pseudocolor for Cy5.5: scarlet).

4.8 Endometriosis model

All experiments were performed according to the institutional Guide for the Care and Use of Laboratory Animals and were approved by the institution's animal care and use committee. Modeling surgery was performed in the estrus of SD rats shown by vaginal smears. After anesthesia, the rats were fixed on a surgical plate by intraperitoneal injection of 10% chloral hydrate (0.35 mL/100 g). The rats were placed in the supine position, and their lower abdomen was skinned and disinfected. A longitudinal incision of approximately 2–3 cm was made about 1.5 cm above the vaginal opening in the middle of the lower abdomen. The anterior bladder and bowel were separated to find the Y-shaped uterus.

One side of the uterus was pulled out with forceps and ligated with ophthalmic suture near the root of the uterus body. Then, it was cut out and put in a disposable medicine bowl containing a small amount of normal saline. The uterus was cut along the long axis and gently scraped for the white endometrial structure in the uterine cavity with a surgical blade dissolved in physiological saline in a disposable medicine bowl. The needle of a 1 mL syringe was replaced with that of a 5 mL syringe, the normal saline mixed with endometrial structure was sucked from the medicine bowl, and then evenly injected into the abdominal cavity. The abdominal cavity was closed layer by layer, and 4.0 mega-units of broad-spectrum penicillin with normal saline were injected intramuscularly daily after surgery to prevent postoperative infection. Estradiol benzoate (0.2 mg kg^{-1}) was intramuscularly injected every 24 h thereafter for 3 days to promote the planting and growth of the ectopic endometrial cells.

4.9 *In vivo* imaging of rats with endometriosis

The established endometriosis rat models (n = 3 per group) were anesthetized with isoflurane (1–2%), and NPBCN aqueous solution (0.08 mM Gd kg^{-1}) was intravenously injected. NPCNs were utilized as the control group. Subsequently, the rats were imaged using a Siemens Prisma 3T MRI system (Siemens Healthcare AG, Erlangen, Germany) equipped with a customized coli (Chenguang Medical Technologies, Shanghai, China) for rat imaging. An axial three-dimensional volumetric interpolated examination sequence (3D VIBE) with water-excited fat suppression was used for the contrast-enhanced imaging study using the following parameters: TR = 11.3 ms, TE = 4.9 ms, field of view = 101 × 120 mm, slice thickness = 0.8 mm, number of slices = 60, matrix dimensions = 432 × 512, resolution = 0.23 × 0.23 × 0.8 mm, number of averages = 2, pixel bandwidth = 268, and acquisition time = 3 min and 17 s. MR images were acquired before and after the intravenous injection of the contrast agents at four different time points (0, 1, 2, 3, 4 and 5 d). Fluorescence imaging of the rats was performed on an IVIS Spectrum CT imaging system (PerkinElmer).

Blinded to the group information, the regions of interest (ROIs; ~0.15 cm^2) were evaluated based on the consensus of two experienced radiologists on a post-processing workstation (Syngo MR B19 system, Siemens Healthcare AG, Erlangen, Germany). After MR imaging, the rats were sacrificed, and their endometriosis lesions were collected. The acquired tissues were fixed in 4% paraformaldehyde solution overnight, decalcified in ethylene diamine tetraacetic acid solution, embedded in paraffin, and cut into various slices, which were subjected to hematoxylin and eosin (H&E) staining and immunofluorescence staining.

4.10 Tissue histopathological analysis

Formalin-fixed samples were embedded in paraffin, cut into 5 μm-thick slices, and stained with H according to the standard hematoxylin and eosin (H&E) staining and immunofluorescence staining procedures. All the secondary antibodies used in immunofluorescence staining were purchased from Affinity Biosciences (Jiangsu, China). Green, red and blue immunofluorescence were imaged sequentially.

4.11 Biocompatibility

9 healthy rats were randomly divided into three groups (three rats per group). After blood collection, all the rats were sacrificed at a certain time point. One group was injected with saline and sacrificed 60 days after injection. After intravenous injection of NPBCNs (0.08 mM Gd kg^{-1}), one group was euthanized in a short (3 d) time as the 3d group, and another group was euthanized after a long (60 d) time. Liver and kidney function indexes and blood routine were evaluated. Additionally, the pathological analysis of the main organs (heart, liver, spleen, lung and kidney), which was performed by an experienced

pathologist, was used to evaluate the *in vivo* toxicity of NPBCNs in a short (3 d) and long (60 d) period.

4.12 Statistics analysis

All data are shown as mean ± SEM or SD. Differences between two groups were tested with the Wilcoxon test. For multiple comparisons, one-way ANOVA was applied with Tukey's multiple comparisons test. All analyses were performed using Prism 9 (GraphPad software, USA). $p < 0.05$ was considered as significant.

Ethical statement

Institutional Administrative Panel on Laboratory Animal Care approved all procedures using laboratory animals, and all experiments were complied with the Guidelines for the Care and Use of Laboratory Animals.

Data availability

All data generated or analyzed during this study are included in the article and additional file.

Author contributions

QZ and SW designed the study, performed the experiments, and were involved in data analysis and interpretation, and wrote the manuscript. YL and ML were involved in data analysis and animal experiments. CL and QL were involved in the study design and MRI protocol. JZ and ZY co-edited the manuscript. All authors read and approved the final manuscript.

Conflicts of interest

The authors have declared that no conflict of interest exists.

Acknowledgements

Qi Zhang and Shiman Wu contributed to this work equally. This work was supported by the National Natural Science Foundation of China (Grant No. 81671732 and Grant No. 82272061) and Shanghai Municipal Health Commission (Grant No. 20224Y0382).

References

1 L. C. Giudice and L. C. Kao, *Lancet*, 2004, **364**, 1789–1799.
2 A. Fukui, C. Mai, S. Saeki, M. Yamamoto, R. Takeyama, T. Kato, Y. Ukita, Y. Wakimoto, A. Yamaya and H. Shibahara, *Am. J. Reprod. Immunol.*, 2021, **85**(4), e13342.
3 G. David Adamson, S. Kennedy and L. Hummelshoj, *J. Endometr.*, 2010, **2**, 3–6.
4 M. Zhang, X. Wang, X. Xia, X. Fang, T. Zhang and F. Huang, *Cell Death Discovery*, 2022, **8**(1), 151.
5 S. A. Missmer, S. E. Hankinson, D. Spiegelman, R. L. Barbieri, L. M. Marshall and D. J. Hunter, *Am. J. Epidemiol.*, 2004, **160**, 784–796.
6 N. Ohashi, R. Aoki, S. Shinozaki, N. Naito and K. Ohyama, *Intern. Med.*, 2011, **50**, 2347–2350.
7 J. Son, D. W. Lee, E. Y. Seong, S. H. Song, S. B. Lee, J. Kang, B. Y. Yang, S. J. Lee, J. R. Choi, K. S. Lee and I. S. Kwak, *J. Korean Med. Sci.*, 2010, **25**, 1372–1374.
8 M. Králíčková, A. S. Laganà, F. Ghezzi and V. Vetvicka, *Arch. Gynecol. Obstet.*, 2020, **301**(1), 1–10.
9 M. Kvaskoff, Y. Mahamat-Saleh, L. V. Farland, N. Shigesi, K. L. Terry, H. R. Harris, H. Roman, C. M. Becker, S. As-Sanie, K. T. Zondervan, A. W. Horne and S. A. Missmer, *Hum. Reprod. Update*, 2021, **27**, 393–420.
10 C. Farquhar, *Br. Med. J.*, 2007, **334**, 249–253.
11 S. W. Guo, *Hum. Reprod. Update*, 2009, **15**, 441–461.
12 Z. Liu, M. Zhao, H. Wang, Z. Fu, H. Gao, W. Peng, D. Ni, W. Tang and Y. Gu, *J. Nanobiotechnol.*, 2022, **20**(1), 170.
13 C. Di Carlo, M. Bonifacio, G. A. Tommaselli, G. Bifulco, G. Guerra and C. Nappi, *Fertil. Steril.*, 2009, **91**, 2315–2323.
14 S. Kamrani, E. Amirchaghmaghi, F. Ghaffari, M. Shahhoseini and K. Ghaedi, *Reprod. Health*, 2022, **19**(1), 100.
15 N. Ferrara, H. P. Gerber and J. LeCouter, *Nat. Med.*, 2003, **9**, 669–676.
16 M. Ovais, S. Mukherjee, A. Pramanik, D. Das, A. Mukherjee, A. Raza and C. Chen, *Adv. Mater.*, 2020, **32**(22), e2000055.
17 H. Zhang, Y. Wu, J. Wang, Z. Tang, Y. Ren, D. Ni, H. Gao, R. Song, T. Jin, Q. Li, W. Bu and Z. Yao, *Small*, 2018, **14**, 1702951.
18 D. Ni, Z. Shen, J. Zhang, C. Zhang, R. Wu, J. Liu, M. Yi, J. Wang, Z. Yao, W. Bu and J. Shi, *ACS Nano*, 2016, **10**, 3783–3790.
19 H. Beygi Nasrabadi, E. Madirov, R. Popescu, L. Štacková, P. Štacko, P. Klán, B. S. Richards, D. Hudry and A. Turshatov, *J. Mater. Chem. C*, 2021, **9**, 16313–16323.
20 J. S. Suk, Q. Xu, N. Kim, J. Hanes and L. M. Ensign, *Adv. Drug Delivery Rev.*, 2016, **99**, 28–51.
21 D. Zhang, R. Zhuang, Z. Guo, M. Gao, L. Huang, L. You, P. Zhang, J. Li, X. Su, H. Wu, X. Chen and X. Zhang, *Theranostics*, 2018, **8**, 1340–1349.
22 H. Xing, S. Zhang, W. Bu, X. Zheng, L. Wang, Q. Xiao, D. Ni, J. Zhang, L. Zhou, W. Peng, K. Zhao, Y. Hua and J. Shi, *Adv. Mater.*, 2014, **26**, 3867–3872.
23 F. Erogbogbo, C. W. Chang, J. L. May, L. Liu, R. Kumar, W. C. Law, H. Ding, K. T. Yong, I. Roy, M. Sheshadri, M. T. Swihart and P. N. Prasad, *Nanoscale*, 2012, **4**, 5483–5489.
24 D. Ni, D. Jiang, H. J. Im, H. F. Valdovinos, B. Yu, S. Goel, T. E. Barnhart, P. Huang and W. Cai, *Biomaterials*, 2018, **171**, 144–152.
25 H. Maeda, J. Wu, T. Sawa, Y. Matsumura and K. Hori, *J. Controlled Release*, 2000, **65**, 271–284.
26 B. Peng, H. Zhan, F. Alotaibi, G. M. Alkusayer, M. A. Bedaiwy and P. J. Yong, *Reprod. Sci.*, 2018, **25**, 540–549.
27 S. Mechsner, J. Bartley, C. Loddenkemper, D. S. Salomon, A. Starzinski-Powitz and A. D. Ebert, *Fertil. Steril.*, 2005, **83**, 1220–1231.
28 B. Peng, F. T. Alotaibi, S. Sediqi, M. A. Bedaiwy and P. J. Yong, *Hum. Reprod.*, 2021, **35**, 901–912.